

# Hydrogen production by catalytic partial oxidation of iso-octane at varying flow rate and fuel/oxygen ratio: From detailed kinetics to reactor behavior

M. Hartmann<sup>a</sup>, L. Maier<sup>b</sup>, O. Deutschmann<sup>a,b,\*</sup>

<sup>a</sup> Institute for Chemical Technology and Polymer Chemistry, Germany

<sup>b</sup> Institute for Nuclear and Energy Technology, Karlsruhe Institute of Technology (KIT), Kaiserstraße 12, D-76128 Karlsruhe, Germany

## ARTICLE INFO

### Article history:

Received 20 April 2010

Received in revised form 20 July 2010

Accepted 24 August 2010

Available online 21 September 2010

### Keywords:

Partial oxidation

Reforming

Octane

Gasoline

Rhodium

Hydrogen

Modeling and simulation

## ABSTRACT

Hydrogen production by catalytic partial oxidation of iso-octane is experimentally and numerically studied over a rhodium/alumina coated honeycomb monolith at millisecond contact times by varying both fuel-to-oxygen ratio and flow rates and at varying flow rates. At fuel rich conditions, the formation of by-products potentially serving as coke precursors is observed. The quantity of by-products strongly depends on the flow rate. Both fuel conversion and hydrogen yield increase with increasing flow rate, i.e., decreasing residence time. This extraordinary behavior of autothermally operated short-contact time reactors can be understood by the interaction of mass and heat transport and chemical reactions. Therefore, an elementary-step-like heterogeneous reaction mechanism is implemented into a two-dimensional flow field description of a single monolith channel, coupled with a heat balance of the entire monolithic structure.

© 2010 Elsevier B.V. All rights reserved.

## 1. Introduction

Hydrogen production from logistic transportation fuels such as gasoline by catalytic partial oxidation (CPOX) is currently of great academic and industrial interest [1–8]. In the last decade, partial oxidation of a variety of gaseous and liquid hydrocarbons to hydrogen and synthesis gas (CO and H<sub>2</sub>) has been studied over rhodium based catalysts. It has been shown that most hydrocarbons can be autothermally converted to syngas over rhodium within milliseconds at operating temperatures usually above 1000 K. Short monolithic honeycomb and foam structures made out of metal oxides usually serve as the catalyst carrier. Due to the short residence time, high fuel throughput and syngas yields can be achieved in compact reactors operated nearly adiabatically. These features make CPOX reactors attractive for on-board supply of hydrogen and reformat fuel from conventional logistic as well as synthetic fuels, which can be integrated into auxiliary power units based on the proton exchange membrane (PEMFC) and solid oxide (SOFC) fuel cells [9].

In CPOX of methane, the short residence time and stability of the methane molecule prevent homogenous reactions in the fluid phase at atmospheric pressure [10–12]. However, for any other heavier fuel, even ethane and propane [13–15], gas-phase reactions at atmospheric pressure are likely at operating temperatures around 1000 °C and contact times on less than 100 ms. Hence, heterogeneous and homogeneous reactions in CPOX of higher hydrocarbons are not only coupled by adsorption and desorption of fuel and oxygen molecules and the products, respectively. The process is also highly determined by the adsorption and desorption of generated intermediates and radicals. Therefore, mass transport of radicals and intermediates from/to the gaseous bulk phase and the catalytically active channel wall, mainly by radial diffusion in the small channels of the monolith being on the order of a quarter to 1 mm, is crucial for the interaction of heterogeneous and homogeneous reactions in CPOX reactors [16]. Furthermore, heat transfer effects become significant for the product composition [17]. For these reasons, optimization and reliable operation of CPOX reactors call for a better understanding of the occurring complex interaction of heterogeneous and homogeneous chemical reactions as well as their coupling with mass and heat transport.

Due to this complexity in chemistry and species transport, the application of detailed models for numerical simulation of CPOX reactors in the literature has only recently been extended from light hydrocarbon fuels such as methane and ethane [10,11,13,18] to liquid fuels [16,19,20]. Our group has developed models for CPOX

\* Corresponding author at: Institute for Chemical Technology and Polymer Chemistry, Karlsruhe Institute of Technology (KIT), Engesserstr. 20, D-76131 Karlsruhe, Germany. Tel.: +49 721 608 3064; fax: +49 721 608 4805.

E-mail address: [deutschmann@kit.edu](mailto:deutschmann@kit.edu) (O. Deutschmann).

of higher hydrocarbons including detailed (elementary step) reaction mechanisms for heterogeneous and homogeneous chemical reactions as well as adequate mass and heat transport models. In a previous paper, a detailed numerical simulation for CPOX of iso-octane over rhodium was conducted [16]. In particular, the formation of undesired by-products and the role of homogeneous gas-phase reactions were considered in this work. Moreover, it has been shown that the formation of soot precursors occurs through homogeneous gas-phase reactions at rich operating conditions and high temperatures. Even if those soot precursors may not harm the CPOX reactor, they present a potential threat for any device further downstream such as fuel cells.

In this paper, we present an experimental and numerical study on the impact of the mass flow rate on conversion, selectivity, and operating temperature in an autothermal short-contact-time reactor at atmospheric pressure. Iso-octane is used as fuel serving as gasoline model component. The fuel is converted over a rhodium/alumina coated honeycomb monolith. Although more complex fuels have already been studied experimentally [19,20,24], the single-component reference fuel iso-octane (i-octane, 2,2,4-trimethylpentane) has been chosen because a detailed heterogeneous reaction mechanism of CPOX of iso-octane over Rh has recently been developed [16]. It is applied in the current study without modification. In addition to the mass flow rate which has been varied between 2 and 6 slpm, the fuel-to-oxygen ratio has been changed from oxygen excess to oxygen deficiency conditions.

Several authors have studied the effect of flow rate on conversion and selectivity in CPOX reactors. For instance, Krummenacher et al. discussed the catalytic partial oxidation of several higher hydrocarbons (e.g. n-decane, n-hexadecane) at short contact times focusing on the influence of the fuel on product distribution [21]. Beyond the scope of this paper, a beneficial effect of high flow rates on hydrogen production was noticed. However, no general trend could be predicted due to overlapping effects such as coking of fuel upstream the catalyst. Seyed-Reihani and Jackson investigated the influence of thermal operation conditions on CPOX of n-butane over supported Rh catalysts [22]. In accordance to the experimental data presented in this work, lower fuel conversions and a trend towards total oxidation were observed at low flow rates and after removal of thermal insulation of the catalytic reactor. Beretta and Forzatti studied the CPOX of ethane and propane under isothermal operation conditions from 500 to 720 °C in an annular reactor [23]. Whereas for platinum catalysts the selected flow rate had no effect on product distribution at constant temperatures, for rhodium, a notable impact was found for intermediate residence times.

## 2. Experimental set-up and measurement procedure

### 2.1. Experimental set-up

Asides from measuring the reactor performance as functions of varying external parameters, a major objective of the employed experimental set-up is the delivery of well-reproducible data for the development and evaluation of detailed chemical reaction models. This implies that the used reactor configuration must guarantee well-defined initial and boundary conditions, which gave guidance for the design of the set-up. The development was supported by CFD simulations of the mixing process, leading to a tube-in-tube configuration that allows a rapid mixing of vaporized fuels with synthetic air to feed the catalyst with a homogeneous, pulse-free mixture at a uniform temperature [19]. Fig. 1 gives a technical illustration of the reactor configuration and the fuel/syn-air mixing process. A detailed description of the experimental set-up is given elsewhere [16].

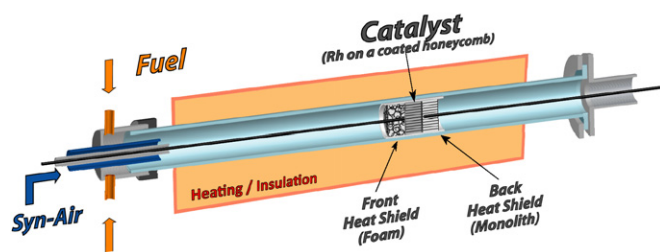


Fig. 1. Sketch of the experimental set-up. The CFD guided development led to a tube-in-tube configuration that allows a rapid mixing of vaporized fuels with synthetic air to feed the catalyst with a homogeneous, pulse-free mixture at a uniform temperature.

All relevant species present in the product stream are detected by a variety of simultaneously applied analytical methods: FT-IR, MS, and a paramagnetic gas analyzer. A combination of these techniques ensures well-closed balances for carbon, hydrogen, and oxygen and permits time-resolved monitoring of at least 12 species on the order of seconds. Further carbon containing species are detected by GC-MS, however with much smaller time-resolution. Typical atom balances that are reached with this combined method were between the following limits:  $94% < H < 101%$ ,  $91% < C < 99%$  and  $98% < O < 103%$ .

### 2.2. Catalyst

An industrially manufactured honeycomb catalyst (900 cells per square inch (cpsi); rhodium loading =  $1.41 \text{ mg/cm}^3$ ) is used. The monolith is made out of cordierite and is 10 mm in length and 19 mm in diameter. The inner channel walls are coated with rhodium dispersed in an alumina washcoat; no further additives are used. The catalyst is positioned 200 mm downstream of the mixture inlet. Upstream and downstream of the catalyst, an uncoated foam monolith ( $\gamma\text{-Al}_2\text{O}_3$ , 85 pores per inch (ppi)) and an uncoated honeycomb monolith (600 cpsi), respectively, are placed close to the catalyst. Both non-catalytic monoliths are 10 mm in length and 19 mm in diameter and are used as heat shields and fixations for thermocouples (front face: Type K, back face: Type N).

### 2.3. Measurement procedure

The C/O ratio is used as parameter for the description of the composition of the mixture entering the catalyst; it is defined as the ratio of the total number of carbon atoms to the total number of oxygen atoms in the inlet mixture. The C/O ratio is varied between 0.8 and 1.3 at a constant dilution with 80 vol.% nitrogen. After light-off, the reactor is operated autothermally, which means the furnace initially used for light-off is switched off. Fuel and synthetic air are fed to the reactor at 463 K (190 °C).

To investigate the effect of residence time on the catalytic partial oxidation of higher hydrocarbon fuels, the total flow rate of the inlet mixture has been varied from 2 to 6 slpm in small steps of 1 slpm. These flows correspond to gas hourly space velocity (GHSV) between  $42\,500 \text{ h}^{-1}$  at 2 slpm and  $127\,000 \text{ h}^{-1}$  at 6 slpm referred to standard conditions (298.15 K, 1013.25 mbar).

After reaching steady state, experimental data is collected for 10–15 min at each C/O ratio. No aging due to sintering or coking of the catalyst could be observed during this period. Steady states could be reached again after completion of all measurements between C/O = 0.8–1.3. No hysteresis is observed.

### 3. Modeling approach and numerical implementation

#### 3.1. Flow field in the catalytic channel

The single catalytically coated channel is approximated by an axis-symmetric cylinder leading to the axial and radial spatial coordinates as independent variables. The basis of the flow field simulations are the Navier–Stokes equations coupled with a governing equation describing the heat transport in the fluid phase. Nine governing equations describe convection, diffusion and chemical reactions of the relevant species as discussed below. Since the residence time in the monolith is on the order of milliseconds, the transport in the axial direction is mainly determined by convection. Therefore, axial diffusion can be neglected reducing the elliptical structure of the steady-state Navier–Stokes equations to a parabolic one by application of a boundary-layer approximation [25–27]. The resulting governing equations are a large system of parabolic partial differential equations (PDEs) with nonlinear boundary conditions arising from the coupling between the gas-phase and the surface processes:

$$\text{Mass continuity : } \frac{\partial \rho u}{\partial z} + \frac{1}{r} \frac{\partial (r \rho v)}{\partial r} = 0, \quad (1)$$

$$\text{Axial momentum : } \rho u \frac{\partial u}{\partial z} + \rho v \frac{\partial u}{\partial r} = -\frac{\partial p}{\partial z} + \frac{1}{r} \frac{\partial}{\partial r} \left( \mu r \frac{\partial u}{\partial r} \right), \quad (2)$$

$$\text{Radial momentum : } 0 = \frac{\partial p}{\partial r}, \quad (3)$$

$$\text{Thermal energy : } \rho c_p \left( u \frac{\partial T}{\partial z} + v \frac{\partial T}{\partial r} \right) = \frac{1}{r} \frac{\partial}{\partial r} \left( r \lambda \frac{\partial T}{\partial r} \right) - \sum_{k=1}^{N_g} c_{pk} J_{k,r} \frac{\partial T}{\partial r}, \quad (4)$$

$$\text{Species continuity : } \rho u \frac{\partial Y_k}{\partial z} + \rho v \frac{\partial Y_k}{\partial r} = -\frac{1}{r} \frac{\partial (r J_{k,r})}{\partial r} \quad (k = 1, \dots, K_g), \quad (5)$$

$$\text{State equation : } p = \frac{\rho R T}{\bar{W}}, \quad (6)$$

$$\text{and } J_{k,r} = -D_k^m \frac{W_k}{\bar{W}} \rho \frac{\partial X_k}{\partial r}, \quad (7)$$

$$\mu = \mu(Y, T), \quad Y = Y_1, Y_2, \dots, Y_{K_g}. \quad (8)$$

Here,  $z$  and  $r$  are the axial and radial coordinates, respectively,  $u$  and  $v$  are the axial and radial components of the velocity vector, resp.,  $p$  is the pressure,  $T$  is the temperature,  $Y_k$  is the mass fraction of species  $k$ ,  $\mu$  is the viscosity,  $\rho$  is the mass density,  $c_p$  is the heat capacity of the mixture,  $\lambda$  is the thermal conductivity of the mixture,  $c_{pk}$  is the species heat capacity of the  $k$ th species,  $K_g$  is the total number of gas-phase species,  $J_{k,r}$  represent the radial components of the diffusive flux vector of  $k$ th species pointing from the center to the wall,  $h_k$  is the heat enthalpy of the  $k$ th species,  $W_k$  is the molar mass of the species  $k$ ,  $\bar{W}$  is the mixture mean molecular weight, and  $R$  is the universal gas constant,  $D_k^m$  is the mixture diffusion coefficient of the  $k$ th species.

At the catalytic surface, the gaseous species mass flux produced by heterogeneous chemical reactions is balanced by the mass flux of that species in the gas phase at the gas–surface interface, i.e.,

$$\eta F_{\text{cat/geo}} \hat{s}_k W_k = -J_{kr} \quad (k = 1, \dots, K_g), \quad (9)$$

where

$$\hat{s}_k = \sum_{i=1}^{N_s} \nu_{ik} k_{fi} \prod_{j=1}^{K_g+K_s} c_j^{\nu'_{jk}} \quad (10)$$

is the creation or depletion rate of gas phase ( $k = 1, \dots, K_g$ ) and surface ( $k = K_g+1, \dots, K_g+K_s$ ) species due to the adsorption and desorption on/from the catalytic surface and reactions among surface species;  $K_s$  is the total number of adsorbed (surface) species including a vacant adsorption site species,  $N_s$  is the number of all reactions involving the catalyst;  $c_j$  are species concentrations, and  $\nu_{ik}$  are the stoichiometric coefficients of the reaction equations. The factor  $F_{\text{cat/geo}}$  describes the ratio of catalytic active to geometric surface area, which corresponds to the amount of catalyst available for surface reactions. In this work,  $F_{\text{cat/geo}}$  was experimentally determined to be 15 by CO chemisorption measurements. The effect of finite diffusion in the washcoat on the reaction rate is treated by adding an effectiveness factor,  $\eta$ , into the boundary conditions (Eq. (9)). The effectiveness factor is an algebraic expression in terms of the Thiele modulus and can be computed along with the surface reaction rates. Since the washcoat layer is thin in the monolith used here, the effectiveness factor is close to unity. For more details, we refer to a recent study on the impact of washcoat diffusion on mass transport in monolithic catalysts [28].

Eq. (10) is also applied to calculate the creation or depletion rate of adsorbed species and the surface coverage,  $\theta_k = c_k \sigma_k / \Gamma$ , with  $\Gamma$  and  $\sigma_k$  being the surface site density and the number of sites occupied by adsorbed species  $k$ , respectively. The forward rate coefficient  $k_{fi}$  of surface reaction  $i$  is calculated by a modified Arrhenius expression,

$$k_{fi} = A_i T^{\beta_i} \exp\left(-\frac{E_{ai}}{RT}\right) \prod_{k=1}^{K_s} \theta_k^{\mu_{ki}} \exp\left(\frac{\varepsilon_{ki} \theta_k}{RT}\right), \quad (11)$$

where  $\mu_{ji}$  and  $\varepsilon_{ji}$  are parameters describing an additional dependence of the rate coefficients on the surface coverage [25,29].

In the steady-state, all adsorbed species (surface species) will obey a non-linear algebraic equation system

$$\hat{s}_k = 0 \quad (k = K_g+1, \dots, K_g+K_s). \quad (12)$$

The resulting PDEs are semi-discretized by a method of lines leading to a large-scale, structured, differential algebraic equation (DAE) system, which is solved using the computational code DETCHEM<sup>CHANNEL</sup>; for more details, we refer to [22–24,30].

#### 3.2. Modeling the heat transfer in the catalytic monolith

Due to the thermal insulation shielding the monolith, the radial temperature gradient across the catalyst is small. Since uniform inlet conditions are ensured, all channels of the monolith behave essentially alike. In this case, only one representative channel needs to be analyzed. However, heat losses due to radiation, in particular of the front and back side of the catalytic monolith, may have a severe effect on the temperature profile. The amount of heat loss primarily depends on the temperature of the solid structure of the catalyst. Therefore, we also model the heat transfer of the catalytic monolith in this study.

Individual channels are combined into a transient temperature model for the monolithic bulk. The temperature field of the monolith is treated as a homogeneous continuum in two dimensions. The evolution of the transient temperature field  $T$  can be written as:

$$\rho c_p \frac{\partial T}{\partial t} = -\frac{\partial}{\partial x_i} \Phi_{H,i} + q_H, \quad (13)$$

with  $\rho$  effective density of the monolith,  $c_p$  specific heat capacity,  $\Phi_H$  heat flux vector, and  $q_H$  heat source term due to heat trans-

fer between solid bulk and with fluid flow in the channels at the gas–surface interface. The diffusive heat flux inside the monolith is modeled by anisotropic heat conduction

$$\Phi_{H,i} = -\lambda_{ij} \frac{\partial T}{\partial x_j}, \quad (14)$$

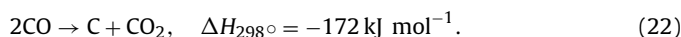
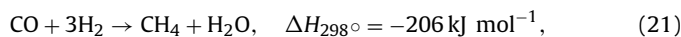
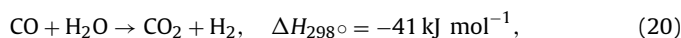
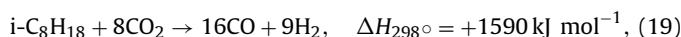
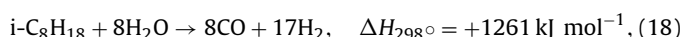
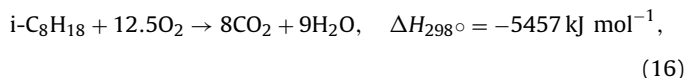
where the heat conduction coefficient  $\lambda$  can take different values for the axial and radial directions. The modeled reactor may consist of several layers with different material properties to account for insulation, etc. All properties are functions of temperature. A fixed temperature or arbitrary heat fluxes including terms for conduction, convection, or radiation can be defined as boundary conditions. The heat source terms are calculated during the simulation of the gas-phase flow through the channels. The heat transfer from the gas phase into the solid or vice versa is indicated by a change of the integral enthalpy flux  $\dot{H}_{\text{gas}}$  in the gas phase:

$$q_H = -\sigma \frac{\partial \dot{H}_{\text{gas}}}{\partial x_1}. \quad (15)$$

The channel density  $\sigma$  denotes the number of channels per unit area of the cross-section. Since the numerical simulation of the fluid flow is the most time consuming step, not every possible channel is simulated in detail. A representative number of channels needs to be considered only. Using a cluster algorithm the choice of representative channels can be conducted efficiently [30]. This approach is realized in the computer code DETCHEM<sup>MONOLITH</sup> [31], which uses the code DETCHEM<sup>CHANNEL</sup> for the simulation of the individual channels.

### 3.3. Surface reaction mechanism

Several global reactions have to be considered in partial oxidation of logistic fuels reaching from total oxidation (Eq. (16)) versus partial oxidation (Eq. (17)), steam and dry reforming (Eqs. (18) and (19)) to water gas shift reaction (Eq. (20)), methanation (Eq. (21)), carbon deposition (e.g. by the Boudouard reaction, Eq. (22)), pyrolysis (e.g. formation of ethylene), and molecular weight growth, i.e., formation of soot and soot precursors. Using *i*-octane as example, those reactions can be written as:



These reactions may not only occur on the catalytic surface but also in the gas phase due the high operating temperatures. In particular, pyrolysis and the formation of soot precursors and soot are expected to occur in the gas-phase [16]. The only way to really understand the reaction complexity of reforming of higher hydrocarbons is the application of chemical models that are based on the molecular behavior as much as possible. Therefore, the current study applies elementary-step-like reaction mechanisms for the catalytic conversion. Since the scope of this work is about the understanding of the impact of flow rate on temperature, conversion and product selectivity, we keep the system as simple as possible in the presented study. For these reasons, gas-phase reactions are not considered and a detailed surface reaction mechanism is applied in the chemistry model only. In former studies [16,19] we

could show that homogeneous conversion only occurs at C/O ratios above unity in CPOX of *i*-octane leading to pyrolysis subsequently followed by formation of soot precursors and soot. For interpretation of experimental data, we here present modeling results for C/O equal or smaller than unity.

The surface reaction model is taken from our former study [16] without any modification. This model for heterogeneous partial oxidation of *i*-octane on the rhodium-based catalysts uses a detailed surface reaction scheme for partial oxidation of C<sub>1</sub>–C<sub>3</sub> species coupled with two additional “lumped” reactions for adsorption of *i*-octane assuming that *i*-octane adsorption quickly leads to the species that are explicitly described by the detailed part of the mechanism. The detailed surface reaction mechanism consists of 56 reactions among 9 gas-phase and 17 surface adsorbed species. The detailed mechanism coupled with the global reactions describes all global reactions (Eqs. (16)–(22)) via a complex reaction network except olefin production and soot formation, which are unlikely to occur heterogeneously. The mechanism includes steps that can lead to a monolayer of carbon.

## 4. Results

The presented yield  $Y_P$  of the product species  $P$  is calculated in terms of the measured reactor outlet flow rates of molar C or H in the product species  $P$  divided by the molar inlet carbon or hydrogen, flow rates referring to the fuel:

$$Y_P^H = \frac{v_P^H \dot{n}_P}{v_{\text{Fuel}}^H \dot{n}_{\text{Fuel}}^{\text{In}}} \quad \text{and} \quad Y_P^C = \frac{v_P^C \dot{n}_P}{v_{\text{Fuel}}^C \dot{n}_{\text{Fuel}}^{\text{In}}}, \quad (23)$$

with  $v_{P,\text{Fuel}}^{\text{H,C}}$  = number of H or C atoms in the product species  $P$  or in the fuel,  $\dot{n}_{\text{Fuel}}^{\text{In}}$  and  $\dot{n}_P$  = inlet fuel and outlet product molar flow rate. Therefore,  $Y_P$  describes the molar distribution of carbon or hydrogen in the product spectra after the reaction.

Fig. 2 presents the yields of hydrogen and water over the investigated range of space velocities and C/O ratios. In general, towards oxygen rich inlet feeds with C/O < 1.0, total oxidation of the fuel is favored. For all space velocities, the maximum of hydrogen production is observed at C/O = 1.05. However, the H<sub>2</sub> yields as function of C/O ratio are varying with the selected flow rate. At longer residence times ( $V_{\text{total}}^{\text{in}} = 2 - 3$  slpm; GHSV = 42 500–63 000 h<sup>-1</sup>), higher H<sub>2</sub>O yields are observed, indicating a trend towards more total oxidation. For space velocities faster than 4 slpm (GHSV = 85 000 h<sup>-1</sup>) a limitation in the production of both hydrogen and water is observed. However, an increase in space velocities from 4 to 6 slpm (GHSV = 85 000 h<sup>-1</sup>–127 000 h<sup>-1</sup>) results in a constant yield of  $Y_{\text{H}_2}^H = 0.94$  at C/O = 1.05 for hydrogen and  $Y_{\text{H}_2\text{O}}^H = 0.04$  at C/O = 1.05 for water production. In comparison to the generation of hydrogen, the minimum in water yield is slightly shifted towards fuel rich C/O ratios. For space velocities ranging from 4 to 6 slpm, the minimum of yielded water is reached at C/O = 1.1 ( $Y_{\text{H}_2\text{O}}^H = 0.021$ ) and at C/O = 1.2 ( $Y_{\text{H}_2\text{O}}^H = 0.04$ ) for 3 slpm, respectively. The minimum for the slowest tested space velocity of  $V_{\text{total}}^{\text{in}} = 2$  slpm is not reached within the range of investigated reactant compositions of C/O ≤ 1.3.

Fig. 3 displays the measured temperature at the catalyst outlet. Overall, the temperature is increasing under oxygen rich conditions whereas under fuel rich conditions a decline in the catalyst exit temperature can be observed for all tested contact times. Both the magnitude of temperature changes and the point of inflexion at C/O = 1.0–1.3 are correlated to the slope and minimum water production according to the highly exothermic reaction enthalpy of the total oxidation reaction. However, besides equal rates for water and hydrogen production for flow rates from 4 to 6 slpm (GHSV = 85 000 h<sup>-1</sup>–127 000 h<sup>-1</sup>) a parallel shift in the catalyst exit

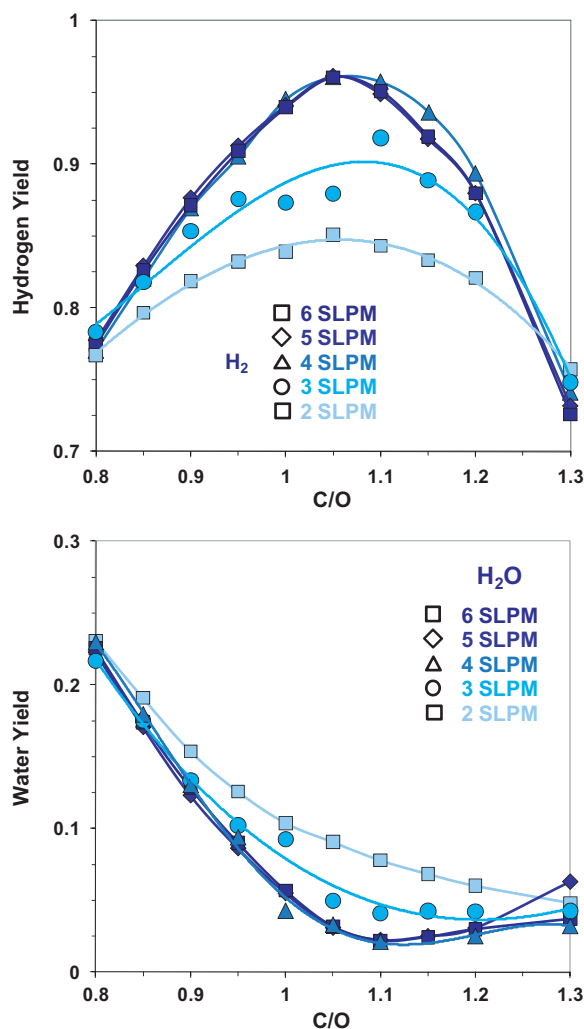


Fig. 2. Measured H atom based yields of  $H_2$  and  $H_2O$  in CPOX of *i*-octane as function of flow rate and C/O ratio.

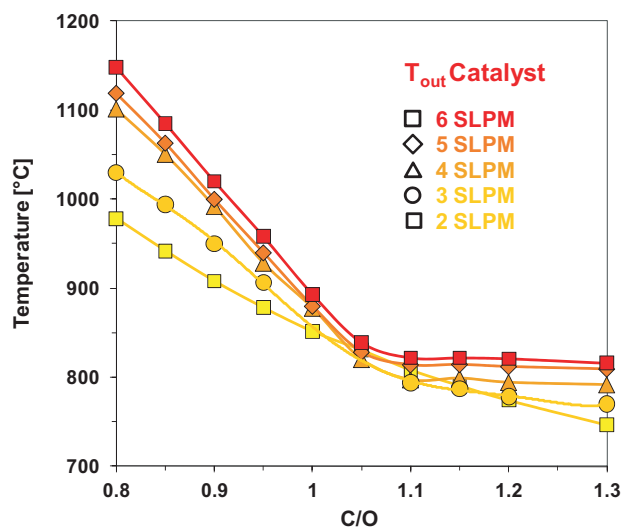


Fig. 3. Measured catalyst outlet temperatures in CPOX of *i*-octane as function of flow rate and C/O ratio.

temperature is recorded. The temperature increases by approximately 10–14 K over the entire investigated range of C/O ratios by an increase from 4 to 5 slpm (GHSV 85 000–105 800  $h^{-1}$ ) and from 5 to 6 slpm (GHSV 105 800–127 000  $h^{-1}$ ), respectively.

Fig. 4 presents the experimentally determined yields of the by-products methane, ethylene, and propylene as well as the total sum of hydrocarbons at the reactor exit including unconverted fuel. The experiments reveal that for low space velocities between 2 and 3 slpm (GHSV = 42 500–63 000  $h^{-1}$ ), a full conversion of the injected fuel cannot be reached even if an excess of oxygen is available (Fig. 5). In general, one would assume that conversion increases with residence time, but here, we clearly see a decrease of conversion with increasing residence time, which will be discussed below. Correspondingly, an increase in the production of the thermal decomposition products methane, ethylene and propylene is observed. For flow rates exceeding 4 slpm (GHSV > 85 000  $h^{-1}$ ) complete fuel conversion is reached under oxygen rich condition. No generation of any thermal cracking products is observed at these contact times. At closed balances,  $H_2$  and  $H_2O$  are the only detected reaction products. However, emerging at stoichiometric reactant composition of C/O = 1.0, the yields of cracking products are intensively increasing. At C/O = 1.15 the level of methane, ethylene, propylene production at high flow rates ( $V_{total}^{in} > 4$  slpm; GHSV > 85 000  $h^{-1}$ ) is exceeding those at low flow rates. Proportional ratios of propylene and ethylene yields are found over the entire range of observed C/O ratios and space velocities.

## 5. Discussion

The results reveal that the residence time (flow rate) has a significant impact on fuel conversion, hydrogen yield, formation of by-products, and the catalyst outlet temperature. It is also clearly shown that longer residence times do not favor higher conversion and hydrogen yields. Actually, the reactor performance improves with increasing flow rates, which means with decreasing residence time, at least up to the values studied here. Indeed, the maximum fuel conversion and hydrogen yield, as well as the minimum formation of undesired by-products is achieved at high flow rates. This behavior will be discussed in the remainder using detailed transport and chemistry models and the computer package DETCHEM. Due to the large amount of parameters studied, it will be focused on the C/O ratio of 0.8.

### 5.1. Reaction analysis in the single channel

The principal behavior of fuel conversion in the Rh coated monolith channel is exemplarily shown in Fig. 6 for the case of C/O = 0.8 and a flow rate of 4 slpm. A full heat balance of the monolith is simulated providing the surface temperature profile of the channel. A channel positioned in the centerline of the monolith was chosen. The measured gas-phase temperature at the intersection between the upstream heat shield and the catalyst was chosen to have an inlet temperature of 625 K.

The gas-phase temperature increases rapidly and reaches the solid temperature of the monolith in approximately 1 mm. The highest temperature is predicted at the leading edge of the catalytic channel wall reaching 1504 K. In this first section, total catalytic oxidation of the fuel leads to the formation of water, CO as intermediate species, and  $CO_2$ ; very little hydrogen is formed. Close to the surface, the oxygen, but also almost all the fuel, is consumed, leading to strong radial but also axial concentrations gradients; the overall reaction here is obviously mass-transfer limited. The rate determining step is the diffusion of oxygen towards the catalytically coated wall. Within 1.5 mm, all the oxygen is consumed, even in the bulk fluid. In this region, the water concentration reaches

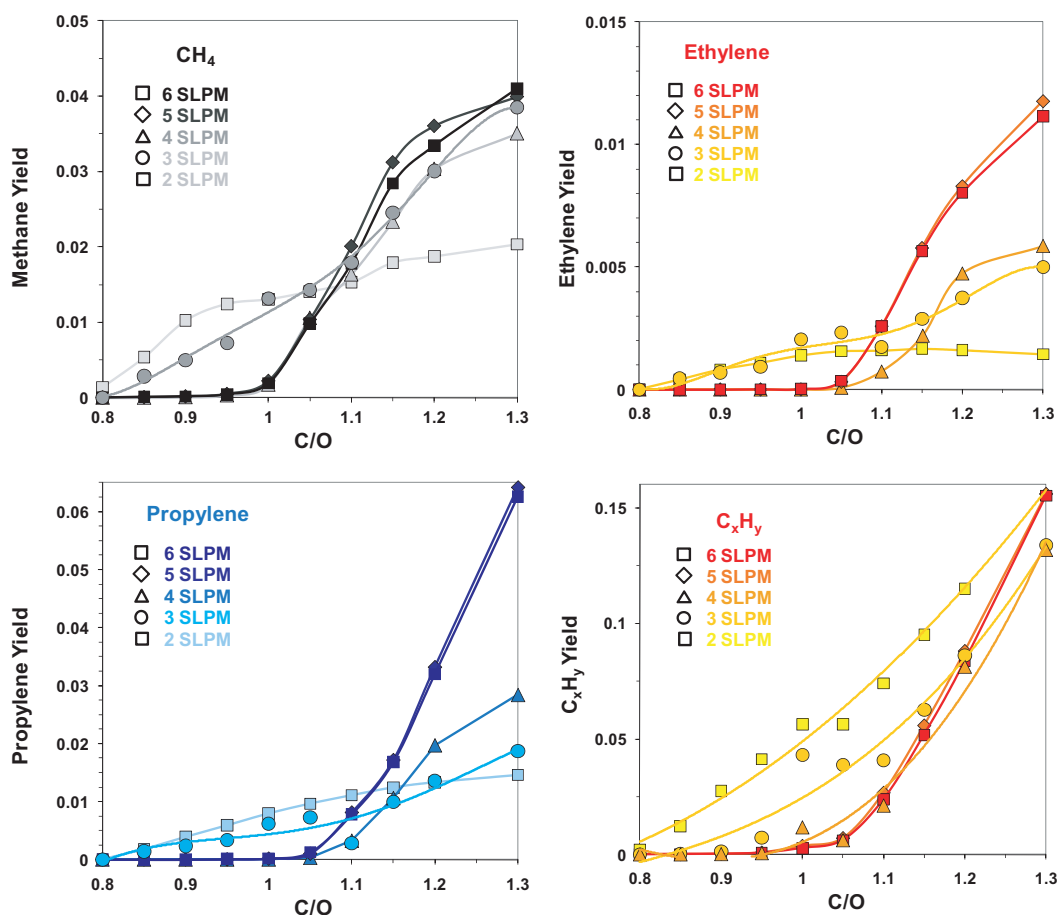


**Fig. 4.** Measured C atom based yield of the cracking products methane, ethylene, propylene as well as total  $C_xH_y$  yield in CPOX of *i*-octane as function of flow rate and C/O ratio.  $C_xH_y$  denotes all hydrogen-atom-containing products including unconverted fuel and thermal cracking products.

its maximum. In the next millimeter, the remaining fuel is steam reformed, consuming water again and producing hydrogen. Since steam reforming is endothermic, the temperature decreases again. The temperature reaches a local minimum at  $z = 4$  mm. Also, in that region the remaining fuel is fully converted. Further downstream, the hydrogen concentration, but also the  $CO_2$ , continues to rise

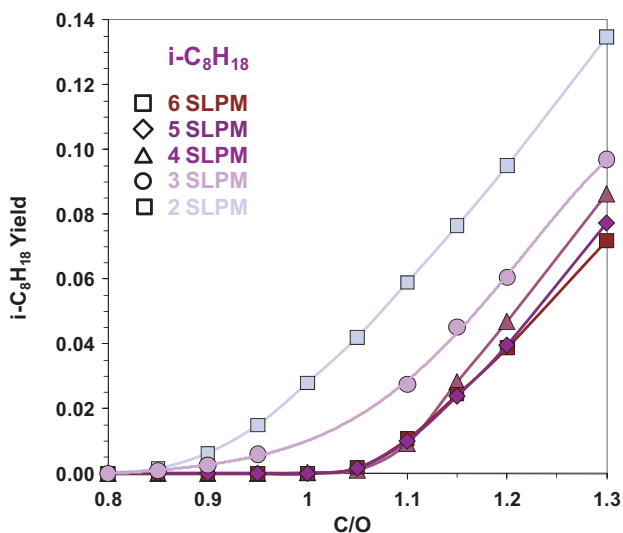


**Fig. 5.** Unconverted *i*-octane in the exhaust stream displayed as C based yields as function of flow rate and C/O ratio.

and the steam and CO concentrations decrease, the water-gas-shift (WGS) reaction plays the decisive role here. Since WGS is a rather slow kinetically controlled process, only weak radial and axial profiles occur. The temperature in the gas-phase slightly increases again due to the exothermicity of WGS, even though there is an overlapping effect due to the heat loss of the monolith as discussed below. These results agree well with the conclusions of Donazzi et al. [31] reporting independent kinetics of direct and reverse WGS reactions when the system is far away from equilibrium, which also is the case for the conditions studied in the present paper. These findings show that the question of fast or slow equilibration of the WGS reaction depends on the operating conditions, i.e., WGS of CPOX of hydrocarbons over Rh may be well-equilibrated at different partial pressures and temperatures as discussed by Wei and Iglesia [32].

In contrast to the central channels of the monolith, the more exterior channels of the monolith have a continuously decreasing gas-phase temperature (not shown here). Summarizing, catalytic partial oxidation is here realized by (almost) subsequent total oxidation, steam reforming, and water-gas-shift.

The computed surface coverages shown in Fig. 7 can be interpreted by the same reaction sequence. Most of the surface is vacant at high temperatures. At the catalyst entrance, oxygen is the primary adsorbate leading to total oxidation. Further downstream, adsorbed oxygen originates from re-adsorbed water molecules and is involved in the steam reforming and water-gas-shift reactions. The primary adsorbates are CO and atomic hydrogen, the later one recombines to produce the desired molecular hydrogen.

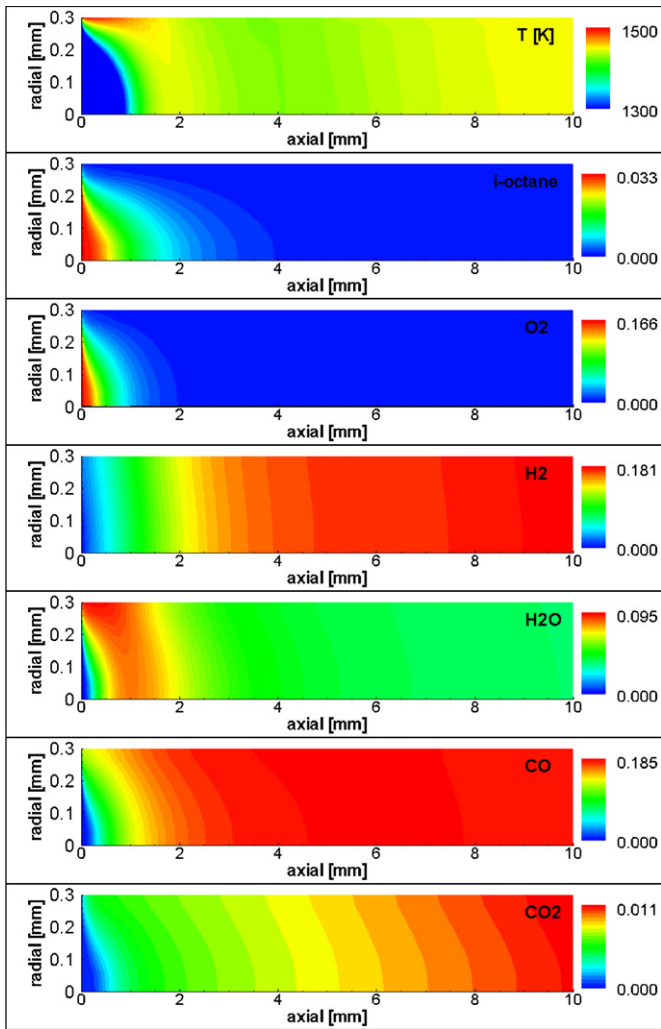


**Fig. 6.** Numerically predicted gas-phase temperature profile and mole fractions of iso-octane,  $O_2$ ,  $H_2$ ,  $H_2O$ ,  $CO$ , and  $CO_2$ , in the catalytic channel at  $C/O=0.8$  and 4 slpm. The symmetry axis of the channel and the gas-wall interface are at  $r=0$  and 0.3 mm, respectively.

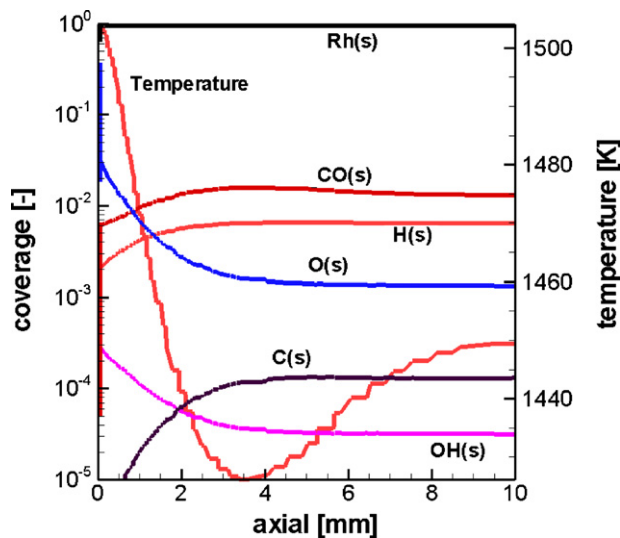


**Fig. 7.** Numerically predicted surface coverage and surface temperature along the channel wall at  $C/O=0.8$  and 4 slpm.

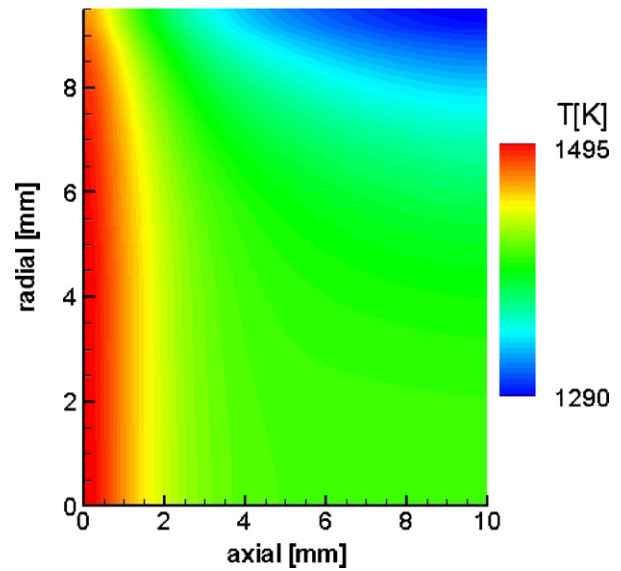


**Fig. 8.** Numerically predicted steady-state monolith temperature at  $C/O=0.8$  and 4 slpm. The symmetry axis of the monolith is at  $r=0$ ; the flow direction is from left to right.

## 5.2. Temperature field in the catalytic monolith

The computed temperature of the solid structure is shown in Fig. 8, again for the reference case of  $C/O=0.8$  and 4 slpm. The simulation includes radiative heat losses at the front and back side of the catalytic monolith and heat conduction at the monolith–thermal insulation interface. Those heat losses lead not only to radial temperature profiles but also to a significant temperature decrease in axial direction. In particular, the channels closer to the exterior wall will experience lower temperatures, which also have an impact on conversion and selectivity. This effect becomes stronger with increasing residence time, i.e., decreasing mass flow rate, because the ratio of the overall heat release due to the exothermic CPOX to the heat loss to the environment decreases with increasing residence time. A second effect is that at high flow rates the reaction zone moves a bit further downstream. Hence, the radiation losses at the front side of the catalyst decrease slightly.

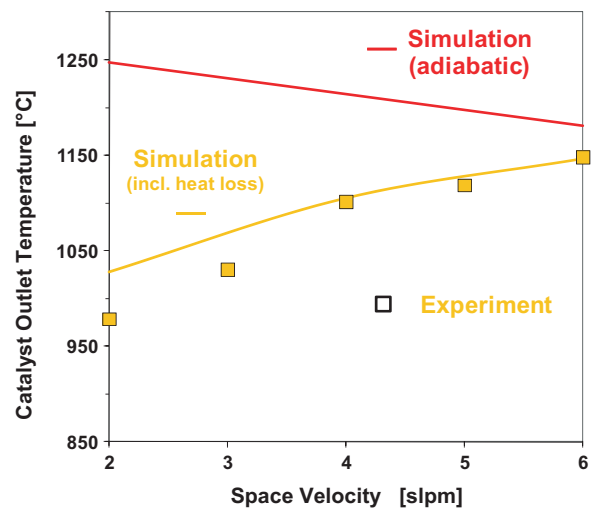


**Fig. 9.** Catalyst outlet temperature as function of space velocity at a given  $C/O=0.8$ ; experimental data versus simulation. (a) single channel simulation without heat losses, (b) monolith simulation with heat losses.

In Fig. 9, the experimentally determined outlet temperature and the numerically predicted outlet temperatures using different models are compared. The first model applies a single channel simulation with adiabatic boundary conditions. The inlet temperature is taken from the experiment measured slightly upstream the interface between the front foam and the catalytic monolith. The second model is exactly the one described above, in which an entire monolith was simulated. Here, heat losses at all monolith boundaries are taken into account (Fig. 8). The temperature displayed in Fig. 8 originates from averaging over the predicted back side of the monolith. Even though one may argue that the measured inlet and outlet temperatures definitely will have some uncertainties due to an imprecise thermocouple position and potential differences between gas-phase and solid temperatures and that the model heat loss parameters such as emissivity, reference temperature, thermal conductivity, and inlet temperature are difficult to estimate, significant conclusions can be drawn from the results.

First of all, the temperature trend in the adiabatic case is opposite to the one observed; the outlet temperature decreases with increasing flow rate, which can be understood by the reaction sequence discussed above. Since the slow, slightly exothermic WGS reaction is the last step after very rapid, strongly exothermic total oxidation and still fast but slightly endothermic steam reforming (Fig. 8), temperature increases with increasing residence time. The highly coated catalyst used in the present study is very active. Pushing the flow rate to much higher values or using a significantly less active catalyst would eventually lead to an increase in the catalyst temperature, because WGS would not occur in the catalyst zone, and the endothermic reforming step would be the last reaction occurring on the catalyst. In that case, higher flow rates would lead to less reforming and consequently to higher temperatures. This behavior at extremely high flow rates has been described in CPOX of methane over Rh, for instance [33]. This temperature increase with flow rate is really caused by the reaction sequence and not by heat losses as discussed below, which is also proven by fuel and oxygen breakthrough [32].

However, in the current paper, the flow rates were moderate. Here the impact of heat losses is much stronger. The outlet temperature predicted by the model that accounts for the heat loss effects agrees qualitatively rather well with the experimentally determined ones. Actually, more precise simulations including detailed simulation of the heat balances in the front and back heat shields (Fig. 1) and using improved estimates of heat transfer parameters [34,35] may also lead to a very good quantitative agreement between model and experiment. However, in the light of the given uncertainties of the temperature measurements, it does not seem necessary to discuss the observed results. The increase in temperature with increasing flow rate observed in this study can simply be understood by the effect of heat losses. The total amount of heat released by the reaction almost linearly increases with flow rate, because fuel is fully converted in the first zone of the catalyst. However, since higher temperatures favor the less exothermic partial oxidation over the highly exothermic total oxidation, there is a kind of self-limiting process concerning the temperature increase. Consequently, the temperatures do not increase extraordinarily with increasing flow rate. The total amount of heat losses to the ambient by thermal conduction and radiation mainly depends on the temperature of the solid structure, which indeed is higher, but not so much higher to compensate for the larger heat release effect. Summarizing, the ratio of chemical heat release to thermal heat loss increases with increasing flow rate, and therefore the temperature increases.

As shown in Fig. 8, the more exterior channels exhibit lower temperatures, which consequently has an impact on the concentration profiles in the individual channels, not all channels behave essentially alike. Hence, a single-channel simulation would not be

able to present the behavior of the entire monolith. However, due to this self-regulating process discussed above, it was seen (experimentally and numerically) that conversion and selectivity did not change significantly when we used the different models; even a single channel simulation at isothermal conditions using the measured outlet temperature led to a very similar product composition, at least for the case of  $C/O = 0.8$ .

Even though the outlet temperature differs by almost 200° for the flow rate variation considered, the exit composition barely changes at  $C/O = 0.8$  (Figs. 2–5). Analogous to the discussion above, this behavior can be explained by a detailed analysis of chemical reaction pathways and heat transfer effects.

The product composition strongly depends on the flow rate at higher  $C/O$  ratios. Remarkably, at  $C/O = 1$  the exit temperatures do not significantly vary with flow rate but the hydrogen yields do. Using the detailed surface reaction mechanisms, 2D single channel, flow field simulations coupled with the monoliths (all three) heat balances, this behavior can be explained. The occurrence of ethylene and other pyrolysis products at  $C/O > 0.8$ , however, can only be explained by taking gas-phase reactions into account, which has been done for isothermal single channel simulations only [16]. The application of the full monolith model is needed to explain the dependencies of those products on flow rate, which is a very demanding computer job and beyond the scope of the current paper.

In general, the generation of hydrocarbon cracking products from initial fuel is very small under oxygen rich conditions. The carbon based yield of all tracked major hydrocarbon fragments such as methane, propylene, and ethylene is not exceeding five percent in total (Fig. 5). However, the increase in reactor temperature due to a relatively decreasing heat loss at higher flow rates is enhancing the endothermic steam reforming of the fuel. As a result, the elevated temperatures lead to total fuel conversion at  $C/O < 1$  and flow rates above 4 slpm. Consequently, no homogenous thermal decomposition products such as methane, propylene, and ethylene can be observed under these operation conditions.

## 6. Conclusions

This combined experimental, modeling, and simulation study led to a much better understanding of the relation between flow rate, chemical heat release, and thermal heat losses in catalytic partial oxidation of iso-octane – serving as a logistic fuel model component – over a rhodium coated monolithic catalyst. A recently set-up laboratory-scale reactor with the associated analysis was used to provide a fundamental data basis, in particular revealing the effect of the flow rate and  $C/O$  ratio on conversion, yield, the formation of soot precursors, and autothermal reactor temperature. Two-dimensional simulations of the flow field in the single catalytic channels coupled with detailed models for heterogeneous fuel conversion can substantially support the understanding of the reaction sequences and help to understand the experimentally observed behavior. Although the simulation-assisted discussion of the experimental behavior was conducted for one  $C/O$  ratio only, it was exemplarily shown how molecular based models can support a better understanding of the reactor behavior.

## Acknowledgements

Fruitful discussions with R.J. Kee (Colorado School of Mines) are very much appreciated. We thank the Umicore AG (Hanau/Germany) for providing the model catalyst. This study was financially supported by the German Research Foundation (DFG).

## References

- [1] A. Lindermeir, S. Kah, S. Kavurucu, M. Muhler, Appl. Catal. A 70 (2007) 488–497.
- [2] B.J. Dreyer, I.C. Lee, J.J. Krummenacher, L.D. Schmidt, Appl. Catal. A 307 (2006) 184–194.
- [3] A.D. Qi, S.D. Wang, C.J. Ni, D.Y. Wu, Int. J. Hydrogen Energy 32 (2007) 981–991.
- [4] R.P. O'Connor, E.J. Klein, L.D. Schmidt, Catal. Lett. 70 (2000) 99–107.
- [5] S. Jain, H.-Y. Chen, J. Schwank, J. Power Sources 160 (2006) 474–484.
- [6] L. Bobrova, I. Zolotarsky, V. Sadykov, V. Sobyenin, Int. J. Hydrogen Energy 32 (2007) 3698–3704.
- [7] J. Thormann, L. Maier, P. Pfeifer, U. Kunz, K. Schubert, O. Deutschmann, Int. J. Hydrogen Energy 34 (2009) 5108–5120.
- [8] L.F. Brown, Int. J. Hydrogen Energy 26 (2001) 381–397.
- [9] C. Severin, S. Pischinger, J. Ogrzewalla, J. Power Sources 145 (2005) 675–682.
- [10] O. Deutschmann, L.D. Schmidt, AlChE J. 44 (1998) 2465–2476.
- [11] R. Quiceno, J. Pérez-Ramírez, J. Warnatz, O. Deutschmann, Appl. Catal. A 303 (2006) 166–176.
- [12] M. Geske, K. Pelzer, R. Horn, F.C. Jentoft, R. Schlögl, Catal. Today 142 (2009) 61–69.
- [13] D.K. Zerkle, M.D. Allendorf, M. Wolf, O. Deutschmann, J. Catal. 196 (2000) 18–39.
- [14] A. Beretta, E. Ranzi, P. Forzatti, Chem. Eng. Sci. 56 (2000) 779–787.
- [15] A. Beretta, L. Piovesan, P. Forzatti, J. Catal. 184 (1999) 455–468.
- [16] M. Hartmann, L. Maier, H.D. Minh, O. Deutschmann, Comb. Flame 157 (2010) 1771–1782.
- [17] R. Schwiedernoch, S. Tischer, C. Correa, O. Deutschmann, Chem. Eng. Sci. 58 (2003) 633–642.
- [18] D. Dalle-Nogare, N.J. Degenstein, R. Horn, P. Canu, L.D. Schmidt, J. Catal. 258 (2008) 131–142.
- [19] M. Hartmann, S. Lichtenberg, N. Hebben, D. Zhang, O. Deutschmann, Chem. Ing. Tech. 81 (2009) 909–919.
- [20] T. Kaltschmitt, L. Maier, M. Hartmann, O. Deutschmann, Proc. Combust. Inst. 33, doi:10.1016/j.proci.2010.05.050.
- [21] J.J. Krummenacher, K.N. West, L.D. Schmidt, J. Catal. 215 (2003) 332–342.
- [22] S.-A. Seyed-Reihani, G.S. Jackson, Appl. Catal. A 353 (2009) 181–192.
- [23] A. Beretta, P. Forzatti, Chem. Eng. J. 99 (2004) 219–226.
- [24] M. Hartmann, T. Kaltschmitt, O. Deutschmann, Catal. Today 147 (2009) S204–S209.
- [25] R. Kee, M. Coltrin, P. Glarborg, Chemically Reacting Flow, 1st ed., Wiley-Interscience, Weinheim, 2003.
- [26] L. Raja, R. Kee, O. Deutschmann, J. Warnatz, L.D. Schmidt, Catal. Today 59 (2000) 47.
- [27] S. Tischer, C. Correa, O. Deutschmann, Catal. Today 69 (2001) 57–62.
- [28] N. Mladenov, J. Koop, S. Tischer, O. Deutschmann, Chem. Eng. Sci. 65 (2010) 812–826.
- [29] O. Deutschmann, in: G. Ertl, H. Knözinger, F. Schüth, J. Weitkamp (Eds.), Handbook of Heterogeneous Catalysis, 2nd ed., Wiley-VCH, Weinheim, 2008, pp. 1811–1828.
- [30] S. Tischer, O. Deutschmann, Catal. Today 105 (2005) 407–413.
- [31] O. Deutschmann, S. Tischer, S. Kleditzsch, V.M. Janardhanan, C. Correa, D. Chatterjee, N. Mladenov, H.D. Minh, DETCHEM™ Software Package, 2.2nd ed., Karlsruhe, 2008, <http://www.detchem.com>;
- A. Donazzi, A. Beretta, G. Groppi, P. Forzatti, J. Catal. 255 (2008) 241–258.
- [32] J. Wei, E. Iglesia, J. Catal. 225 (2004) 116–127.
- [33] K.L. Hohn, L.D. Schmidt, Appl. Catal. A: Gen. 211 (2001) 53–68.
- [34] H. Zhu, R.J. Kee, J.R. Engel, D.T. Wickham, Proc. Combust. Inst. 31 (2007) 1965–1972.
- [35] L. Maier, M. Hartmann, O. Deutschmann, Comb. Flame, submitted.